Identification of Active Magnetic Reconnection Using Magnetic Flux Transport in Plasma Turbulence

Tak Chu Li[1] , Yi-Hsin Liu[1] , and Yi Qi[2]
[1] Department of Physics and Astronomy, Dartmouth College, Hanover, NH, USA; tak.chu.li@dartmouth.edu
[2] Department of Earth, Planetary, and Space Sciences, University of California, Los Angeles, CA, USA

Abstract

Magnetic reconnection has been suggested to play an important role in the dynamics and energetics of plasma turbulence by spacecraft observations, simulations, and theory over the past two decades, and recently, by magnetosheath observations of MMS. A new method based on magnetic flux transport (MFT) has been developed to identify reconnection activity in turbulent plasmas. This method is applied to a gyrokinetic simulation of two-dimensional (2D) plasma turbulence. Results on the identification of three active reconnection X-points are reported. The first two X-points have developed bidirectional electron outflow jets. Beyond the category of electron-only reconnection, the third X-point does not have bidirectional electron outflow jets because the flow is modified by turbulence. In all cases, this method successfully identifies active reconnection through clear inward and outward flux transport around the X-points. This transport pattern defines reconnection and produces a new quadrupolar structure in the divergence of MFT. This method is expected to be applicable to spacecraft missions such as MMS, Parker Solar Probe, and Solar Orbiter.

Unified Astronomy Thesaurus concepts: Solar magnetic reconnection (1504); Space plasmas (1544); Interplanetary turbulence (830)

Supporting material: animation

1. Introduction

Magnetic reconnection and plasma turbulence are both fundamental processes ubiquitously operating throughout the universe. Reconnection has been suggested to contribute to energy dissipation (Dmitruk et al. 2004; Sundkvist et al. 2007; Osman et al. 2011, 2012; Markovskii & Vasquez 2011; Perri et al. 2012; Wan et al. 2012; Karimabadi et al. 2013; TenBarge & Howes 2013; Wu et al. 2013; Zhdankin et al. 2013; Shay et al. 2018) and potential changes in the cascade (Boldyrev & Loureiro 2017; Franci et al. 2017; Loureiro & Boldyrev 2017a, 2017b; Mallet et al. 2017a, 2017b; Vech et al. 2018; Stawarz et al. 2019) of turbulence by in situ observations, numerical simulations and theory. In heliospheric turbulence, reconnection was first observed in situ in the terrestrial magnetosheath by Cluster (Retinò et al. 2007). Recently, high resolution measurements from MMS (Burch et al. 2016) have enabled the detection of electron jets in small-scale current sheets in the turbulent magnetosheath (Yordanova et al. 2016; Vörös et al. 2017; Phan et al. 2018; Wilder et al. 2018), including notably, electron-only reconnection (Phan et al. 2018).

Reconnection occurs in a small-scale electron diffusion region (EDR) within a thin current sheet. As upstream field lines flow into the EDR, they reconnect at the X-point. The reconnected field possesses strong magnetic tension, which drives the reconnected field away from the X-point, ejecting plasma that is coupled to it as bidirectional outflow jets. The fundamental process of reconnection can be described as inward and outward transport of magnetic flux and associated plasmas at an X-point. The transport of magnetic flux and plasma flows across a separatrix was used to define reconnection (Vasyliunas 1975).

At the frontier of turbulence and reconnection research, important questions include how reconnection occurs in a dynamical turbulent system and how the rich dynamics of turbulence and reconnection, such as turbulent energy dissipation

and cascade, interplay. Nevertheless, there is still no clear, reliable method to identify reconnection X-points in turbulent plasmas. In 2D turbulence simulations, the method of saddle points that define an X-point topology was applied (Servidio et al. 2009, 2010; Wan et al. 2013; Haggerty et al. 2017). However, among a large number of identified X-points, only a few displayed significant reconnection electric fields (Servidio et al. 2009). It is possible that many identified X-points are not actively reconnecting.

In observations, a commonly used method to identify reconnection is the detection of bidirectional Alfvénic ion outflow jets. In a turbulent system such as the terrestrial magnetosheath, reconnection can happen at sub-ion or electron scales (Phan et al. 2018; Wilder et al. 2018), and electron jets becomes the conclusive signature of reconnection. However, fast turbulent flows at sub-ion scales can make the detection challenging. In fact, only one out of several tens of sub-ion-scale current sheets detected by Phan et al. (2018) displayed clear bidirectional reconnection electron jets.

Recently, the transport of magnetic flux around an X-point was considered in kinetic simulations of reconnection (Liu & Hesse 2016; Liu et al. 2018). MFT takes into account the decoupling of electron flow and magnetic flux (slippage) arising from a nonideal electric field, and thus correctly captures the inward and outward transport of magnetic flux around a reconnection X-point. In a symmetric reconnection simulation with shear flows, the electron flow can be highly distorted (Liu et al. 2018). Under stronger shear flows or asymmetry, likely in turbulence, the electron flow may not show typical reconnection outflows. In fact, in a highly asymmetric configuration, active reconnection with only one electron jet is possible (Liu & Hesse 2016).

2. Theory

The transport of magnetic flux inherent to reconnection represents an innovative way for identifying active reconnecting

X-points in turbulence. The presence of inward flux transport also indicates reconnection is actively taking place. The MFT velocity U_ψ was previously derived in one and two dimensions (Liu & Hesse 2016; Liu et al. 2018). The key steps leading to the definition of U_ψ are summarized here. In 2D, the magnetic field can be represented as an in-plane and out-of-plane (guide field) component directed along $\hat{z}$: $\boldsymbol{B} = \hat{z} \times \nabla\psi + B_0\hat{z}$. Curling the Faraday's law: $\hat{z} \times [\partial_t\boldsymbol{B} + c\nabla \times \boldsymbol{E} = 0]$ results in $\partial_t\psi = cE_z$. We then consider the electron momentum equation: $\boldsymbol{E} + \boldsymbol{v}_e \times \boldsymbol{B}/c = \boldsymbol{E}'_e$, where $\boldsymbol{E}'_e$ is the nonideal electric field in the electron frame. Taking the z component of this equation and casting it into the form of the 2D advection equation of magnetic flux: $\partial_t\psi + \boldsymbol{U}_\psi \cdot \nabla_\perp\psi = 0$, the in-plane MFT velocity is then given by:

$$\boldsymbol{U}_\psi \equiv \boldsymbol{v}_{ep} - (\boldsymbol{v}_{ep} \cdot \hat{b}_p)\hat{b}_p + \frac{cE'_{ez}}{B_p}(\hat{z} \times \hat{b}_p), \qquad (1)$$

where $\hat{b}_p \equiv \boldsymbol{B}_p/B_p$ is the unit vector of the in-plane magnetic field $\boldsymbol{B}_p$ and $\boldsymbol{v}_{ep}$ the in-plane electron flow. The first two terms represent the in-plane electron flow perpendicular to $\boldsymbol{B}_p$. They come from the $\boldsymbol{v}_e \times \boldsymbol{B}$ term in the electron momentum equation. For $\boldsymbol{E}'_e = 0$, the electron flow is frozen-in to the magnetic field and they move together. When $\boldsymbol{E}'_e \neq 0$, slippage between magnetic flux and electron flow arises as the last term. Without separating the perpendicular electron flow and slippage terms, which provide a relation between the transport of magnetic flux and electron flow, Equation (1) can be simplified to:

$$\boldsymbol{U}_\psi = \frac{cE_z}{B_p}(\hat{z} \times \hat{b}_p). \qquad (2)$$

To the first order in gyrokinetics, U_ψ is given by Equation (1) or (2) with $\boldsymbol{v}_{ep}$, $\boldsymbol{B}_p$, and E'_{ez} replaced by $\delta\boldsymbol{u}_{ep}$, $\delta\boldsymbol{B}_p$, and $\delta E'_{ez} = \delta E_z + (\delta\boldsymbol{u}_{ep} \times \delta\boldsymbol{B}_p/c)_z$, where fluctuating quantities in turbulence are the in-plane electron bulk flow $\delta\boldsymbol{u}_{ep}$ and so on. Note that Equation (1) is not applicable at the X-point because a source or sink term, representing flux generation or annihilation at the X-point, is not included in this advection equation.

A new quantity, the divergence of MFT, $\nabla \cdot \boldsymbol{U}_\psi$, is considered here. $\nabla \cdot \boldsymbol{U}_\psi < 0$ and > 0 can capture the converging inflows and diverging outflows of magnetic flux, respectively. These bidirectional inflows and outflows of magnetic flux at an X-point signifies active reconnection. $\nabla \cdot \boldsymbol{U}_\psi$ also informs about the timescale of diverging magnetic flux from the X-point. Having the dimension of inverse time, $\nabla \cdot \boldsymbol{U}_\psi$ is frame-independent in 2D in the nonrelativistic limit. Therefore, one can compute $\nabla \cdot \boldsymbol{U}_\psi$ for moving X-points without changing frames.

3. Code

The 2D gyrokinetic turbulence simulation has been previously performed (Li et al. 2016) using the the Astrophysical Gyrokinetics Code, or `AstroGK`, described in detail in Numata et al. (2010). `AstroGK` has been extensively used to investigate turbulence in weakly collisional plasmas (Howes et al. 2008; Tatsuno et al. 2009; Howes et al. 2011; TenBarge & Howes 2012, 2013; Nielson et al. 2013; Howes 2016; Li et al. 2016, 2019; Howes et al. 2018) and collisionless strong-guide-field reconnection (Numata et al. 2011; Kobayashi et al. 2014; TenBarge et al. 2014; Numata & Loureiro 2015). `AstroGK` is a Eulerian continuum code with triply periodic boundary conditions. It has a slab geometry elongated along

the straight, uniform background magnetic field, $\boldsymbol{B}_0 = B_0\hat{z}$. The code evolves the perturbed gyroaveraged Vlasov–Maxwell equations in five-dimensional phase space (three-dimensional-two-velocity; Frieman & Chen 1982; Howes et al. 2006). The evolved quantities are the electromagnetic gyroaveraged complementary distribution function for each species s, the scalar potential φ, parallel vector potential $A_\parallel$, and parallel magnetic field perturbation $\delta B_\parallel$, where $\parallel$ is along the total local magnetic field $\boldsymbol{B} = B_0\hat{z} + \delta\boldsymbol{B}$. The total and background magnetic fields are the same to first-order accuracy retained for perturbed fields in gyrokinetics. The velocity grid is specified by pitch angle $\lambda = v_\perp^2/v^2$ and energy $\varepsilon = v^2/2$. The background distribution functions for both species are stationary uniform Maxwellians. Collisions are incorporated using a fully conservative, linearized gyroaveraged Landau collision operator (Abel et al. 2008; Barnes et al. 2009).

4. Setup

The 2D Orszag–Tang Vortex (OTV) problem has been widely used to study plasma turbulence (Dahlburg & Picone 1989; Politano et al. 1989, 1995; Picone & Dahlburg 1991; Grauer & Marliani 2000; Mininni et al. 2006; Parashar et al. 2009, 2014). It is given by

$$\delta\boldsymbol{u} = \delta u[-\sin(k_\perp y)\hat{x} + \sin(k_\perp x)\hat{y}]$$
$$\delta\boldsymbol{B} = \delta B[-\sin(k_\perp y)\hat{x} + \sin(2k_\perp x)\hat{y}],$$

where $\delta u = \delta B/\sqrt{4\pi\rho_0}$, $\delta\boldsymbol{u}$ and $\delta\boldsymbol{B}$ are perturbations in the ion and electron bulk flow and the magnetic field, and $k_\perp = 2\pi/L_\perp$ are positive constants.

To follow the turbulent cascade from the inertial range ($k_\perp\rho_i \ll 1$) to below electron scales ($k_\perp\rho_e > 1$) (TenBarge & Howes 2013; TenBarge et al. 2013, 2014), we specify a reduced mass ratio, $m_i/m_e = 25$, which, in a simulation domain of $L_\perp = 8\pi\rho_i$ and dimensions $(n_x, n_y, n_z, n_\lambda, n_\varepsilon, n_s) = (128, 128, 2, 64, 32, 2)$, enables us to resolve a dynamic range of $0.25 \leqslant k_\perp\rho_i \leqslant 10.5$, or $0.05 \leqslant k_\perp\rho_e \leqslant 2.1$. Plasma parameters are ion plasma $\beta_i = 8\pi n_i T_{0i}/B_0^2 = 0.01$ and $T_{0i}/T_{0e} = 1$. Collision frequencies of $\nu_i = 10^{-5}\omega_{A0}$ and $\nu_e = 0.05\ \omega_{A0}$ (where $\omega_{A0} \equiv k_\parallel v_A$ is a characteristic Alfvén wave frequency in 3D) are sufficient to keep velocity space well resolved (Howes et al. 2008, 2011). Length, time, and velocity are normalized to the ion gyroradius $\rho_i \equiv v_{ti}/\Omega_{ci}$, where $\Omega_{ci} \equiv eB_0/m_ic$, domain turnaround time $\tau_0 \equiv L_\perp/\delta u$ and electron thermal speed $v_{te} \equiv \sqrt{2T_{0e}/m_e}$. τ_0 can be converted to the inverse ion gyro-frequency, a relevant timescale for reconnection, by $\tau_0 = 25\ \Omega_{ci}^{-1}$. The divergence of velocity is normalized to $v_{te}/\rho_e = \Omega_{ce}$.

5. Results

Figure 1(a) shows the out-of-plane current density J_z (color) and contours of the parallel vector potential $A_\parallel$ representing magnetic field lines of the OTV at an early time of $t/\tau_0 = 0.12$. The OTV has an initial flow configuration that rotates the two vortices near the center of the domain, forming a current sheet in between. The symmetry of the two vortices allows symmetric reconnection to take place at the current sheet. The flows also drive two asymmetric vortices at the top right and bottom left, resulting in two mirroring asymmetric reconnection X-points by symmetry of the system. A fourth reconnection X-point, which is a mirror of the central symmetric reconnection X-point, is located at $(x, y) \simeq (0, 12.6)$. The central symmetric (X1) and top right
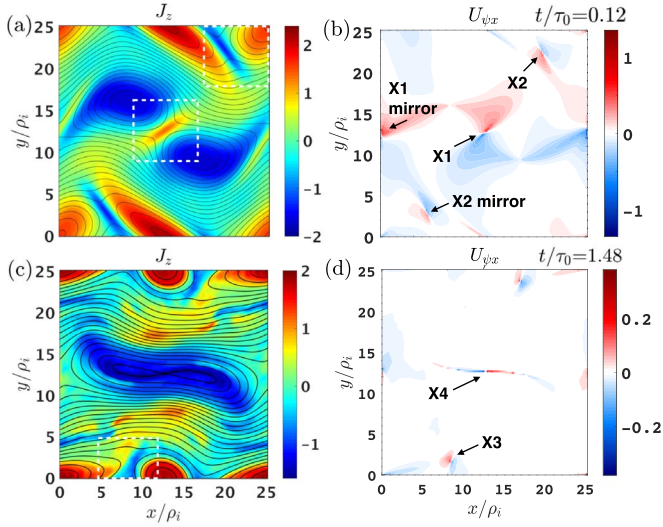
Figure 1. (a) The out-of-plane current density J_z (color) overlaid with contours of $A_\parallel$ of the OTV configuration, and (b) the x-component of U_ψ at $t/\tau_0 = 0.12$, showing X1 and X2 and their mirrors (labeled). At $t/\tau_0 = 1.48$, (c) J_z showing developed turbulence and (d) $U_{\psi x}$ revealing X3, X4 (labeled) and X3 mirror. The bidirectional outflows of magnetic flux at X1 and X4, and inflows at X2 and X3 are observed. δB_p is offset by adding 1% of its maximum value in the domain such that U_ψ remains finite at the X- and O-points that have vanishing δB_p. This does not qualitatively affect the profile of U_ψ. Dashed boxes indicate regions in zoomed-in figures. See an animation of J_z online. The animation lasts for $t/\tau_0 = 0$–2.01. It shows the evolution of reconnection driven by turbulent flows.

(An animation of this figure is available.)

asymmetric (X2) X-points are two of the cases we will discuss in detail.

As the total turbulence energy dissipates over time (Li et al. 2016), the driving of reconnection weakens and reconnection at later times is generally weaker than early-time events. Figure 1(c) shows J_z at late time $t/\tau_0 = 1.48$ when multiscale features, including small-scale current sheets, have developed. A turbulent cascade in the dissipation range (see Figure A1 in the Appendix for the magnetic energy spectrum) is also developed. At this time, an asymmetric reconnection X-point forms at the bottom left. This X-point (X3) does not develop bidirectional electron outflow jets and therefore cannot be identified through electron flows. Below we discuss the application of MFT and the identification of each reconnection X-point.

Figure 1(b) shows the x-component of the MFT velocity, $U_{\psi x}$, of the whole domain at $t/\tau_0 = 0.12$, showing X1 and X2 as well as their mirrors, and (d) at $t/\tau_0 = 1.48$, showing X3, its mirror and a reconnection X-point (X4) formed at the center of an evolved, elongated vortex (flux tube). The factor of δB_p^{-1} in the definition of U_ψ could tend to infinity at the X- and O-points where δB_p vanishes. As a practical step, we add a 1% offset to δB_p everywhere so that U_ψ remains finite at the X- and O-points that have vanishing δB_p. For the range of 0.01%–4% offsets, the amplitudes of U_ψ and $\nabla \cdot U_\psi$ only vary by a factor of 2. Note that masking the X-points by a grid point of size ρ_e yields similar amplitudes to applying a 1% δB_p offset. Below we zoom in to X1–X3 to investigate the X-points more thoroughly.

5.1. X1: Symmetric Reconnection X-point

Figure 2 shows (a) vectors of U_ψ, (b) $\nabla \cdot U_\psi$, and for comparison, (c) vectors and (d) the divergence of δu_e in a zoomed-in region around X1. Clear bidirectional outflows and
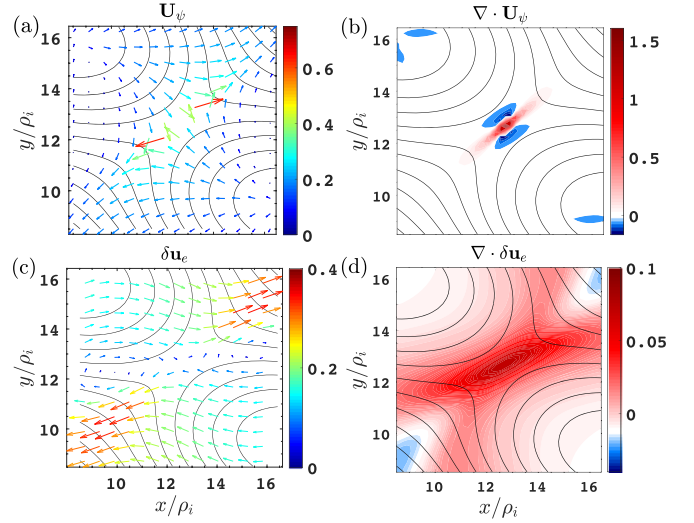

Figure 2. Application of the MFT method to X1, a symmetric reconnection X-point. Plotted quantities are (a) vectors of U_ψ, (b) the divergence of U_ψ, (c) vectors of the fluctuating in-plane electron flow velocity δu_e, and (d) the divergence of δu_e, overlaid with $A_\parallel$ contours. The amplitudes of vectors are denoted by the color and relative length of the arrows. The divergence of velocity is normalized to v_{te}/ρ_e.

converging inflows of magnetic flux around X1 are captured in U_ψ. (b) $\nabla \cdot U_\psi$ reveals negative (blue) and positive (red) amplitudes highly localized to X1, representing converging inward and diverging outward MFT at the X-point. This is the inherent flux transport pattern of reconnection. It results in a new quadrupolar structure in $\nabla \cdot U_\psi$. The quadrupolar structure reflects the bidirectional flux transport at the two sides upstream and downstream of the X-point. Both quantities are highly localized to the X-point, and can serve as local signatures of reconnection.

Bi-directional electron outflow jets in the outflow region can be seen in (c) δu_e. (d) $\nabla \cdot \delta u_e$ reveals positive amplitude, representing the diverging outflows. In comparison to U_ψ, the electron outflow develops further from the X-point and over a much broader region.

5.2. X1: Asymmetric Reconnection X-point

The same quantities as Figure 2 are plotted around X2 in Figure 3. Similarly, clear bidirectional inflows and asymmetric bidirectional outflows of magnetic flux are captured in (a) U_ψ, with the downward transport being stronger. (b) $\nabla \cdot U_\psi$ reveals the presence of converging inward and diverging outward flux transport as $\nabla \cdot U_\psi < 0$ and > 0, respectively, at X2. Both signify active reconnection.

In (c) δu_e, asymmetric electron outflow jets are seen, with a stronger downward jet from X2. (d) The divergence of the electron flow reveals negative and positive amplitudes located broadly around and downstream from the X-point, representing converging inflows and diverging outflows of electrons at this X-point.

5.3. X3: Reconnection X-point without Bidirectional Plasma Jets

As the turbulent flows that drive reconnection are significantly dissipated at late times (Li et al. 2016), reconnection activity becomes weaker than early-time reconnection. Nevertheless, converging inflows and bidirectional outflows of magnetic flux are captured in Figure 4(a) U_ψ at X3. (b) $\nabla \cdot U_\psi$ also reveals positive and negative amplitudes highly
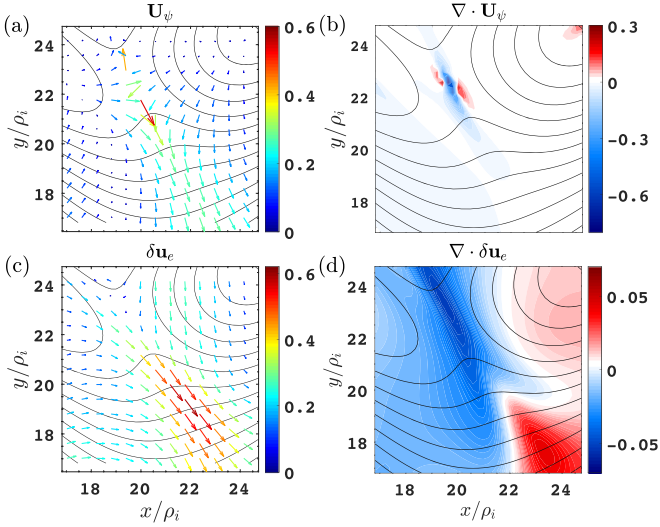
Figure 3. Same quantities as Figure 2 plotted for X2, an asymmetric reconnection X-point.
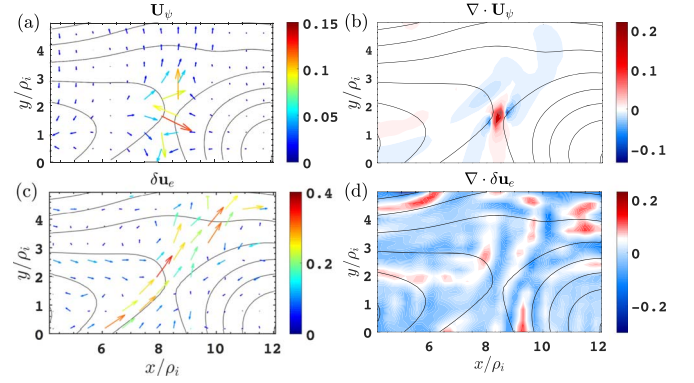

Figure 4. Same format as Figure 2 plotted for X3, a reconnection X-point with only one outflow jet in electrons (and ions), at $t/\tau_0 = 1.48$. Velocity vectors are measured at the X-point frame.
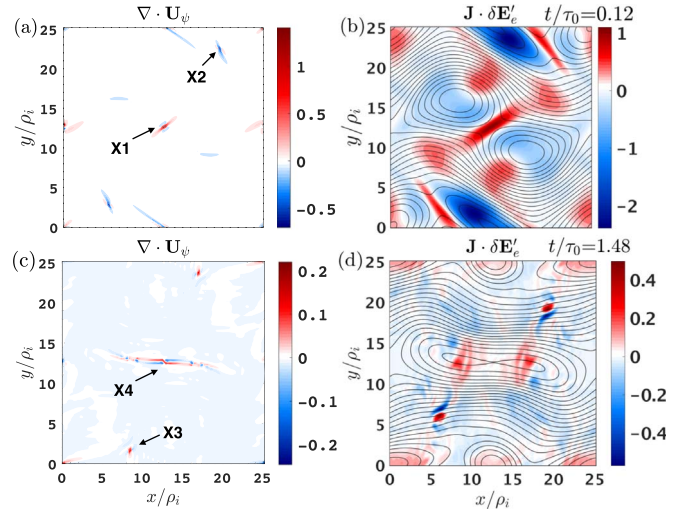

Figure 5. (a) The divergence of MFT of the whole domain at (a) $t/\tau_0 = 0.12$, showing X1 and X2 (labeled) and their mirrors, and (c) $t/\tau_0 = 1.48$, showing X3 and X4 (labeled) among the turbulence; (b) and (d) $\boldsymbol{J} \cdot \delta \boldsymbol{E}'_e$, the nonideal energy conversion in the electron frame, at the two times.

localized to the X-point, sharing a similar quadrupolar structure to X2 and X1.

On the other hand, the electron flow is highly modified by turbulence and previous reconnection events. No clear bidirectional outflow jets are seen in the electrons (or in the ions; see Figure A2 in the Appendix) at X3. Only one electron and one ion outflow jet are present. (d) $\nabla \cdot \delta \boldsymbol{u}_e$ also does not show clear evidence of reconnection. Plasma flows cannot be used for identifying reconnection at this X-point. However, the MFT method is able to identify reconnection through its clear inward and outward flux transport at this X-point, demonstrating the sensitivity of MFT in identifying reconnection activity in turbulence.

5.4. Super-Alfvénic U_ψ

While $\boldsymbol{U}_\psi$ is normalized to v_{te}, it is meaningful to compare it with the upstream Alfvén speed. Using the electron plasma $\beta_e \equiv (v_{te}/c_{Ae})^2 = 0.01$, where $c_{Ae} = \sqrt{B_0/4\pi n_0 m_e}$, in the simulation, and estimates of the upstream $\delta B_p/B_0 \sim 0.1$ and density $n/n_0 \sim 0.7$–1.1 for the three X-points, we can relate the upstream electron Alfvén speed (Cassak & Shay 2007) to v_{te} as $c_{Ae,p}/v_{te} \sim 1$. Therefore, at X1 and X2, U_ψ is of order $c_{Ae,p}$. The flux transport velocity is electron Alfvénic. Similarly, at X3, $U_\psi \sim 1.2\, c_{A,p}$ is super-Alfvénic. The higher velocity at early-time reconnection is associated with strong driving by initial turbulent flows. The Alfvénic velocity at late times is consistent with undriven reconnection simulations (Liu & Hesse 2016). U_ψ is between orders $c_{A,p}$ and $c_{Ae,p}$ based on the simulation.

5.5. Divergence of MFT

Plotted in Figure 5 is the divergence of MFT of the whole domain at (a) $t/\tau_0 = 0.12$, showing X1 and X2 and their mirrors, and at (c) $t/\tau_0 = 1.48$, when turbulence is developed, revealing X3 and X4. $\nabla \cdot \boldsymbol{U}_\psi$ shows significant amplitudes only at the active reconnection X-points, even among the turbulence. It remains small throughout the domain, and is thus suitable for the identification of reconnecting X-points in turbulence. $\nabla \cdot \delta \boldsymbol{u}_e$ is much more structured throughout the system, and at late times, becomes highly turbulent (not shown). For comparison, (b) $\boldsymbol{J} \cdot \delta \boldsymbol{E}'_e$, energy conversion (Zenitani et al. 2011) in the electron frame, is much more broadly distributed over the current sheets

and throughout the system. (d) At late times, it is dominated by turbulent flows far away from the reconnection X-points, and thus may not help in locating reconnection in turbulence. The amplitude of $\nabla \cdot \boldsymbol{U}_\psi$ is of order 0.1–$1\ \Omega_{ce}$ at the three reconnection X-points.

6. Discussion

The flux transport velocity has been generally considered as the $E \times B$ drift velocity. In Equation (1), the slippage between magnetic flux and electron flow arising from an nonideal electric field $\boldsymbol{E}'_e$ is included. For the three reconnection X-points, the slippage provides the major contribution to the inflows and outflows of magnetic flux near the X-point, being ~ 2–3 times larger than the perpendicular electron flow. Further away from the X-point where the the slippage becomes small, $\boldsymbol{U}_\psi$ follows the perpendicular electron flow, which is mainly the $E \times B$ drift.

$\nabla \cdot \boldsymbol{U}_\psi$ consistently shows a quadrupolar structure at all reconnection X-points in turbulence. However, a signal is possible at O-points, where magnetic flux annihilation could happen. This process is recently explored by MMS (Hasegawa et al. 2020). MFT activity at O-points deserves future investigation.

A new category of reconnection in turbulence beyond electron-only reconnection (Phan et al. 2018) is revealed by

X3. Only a single electron Alfvénic electron jet and Alfvénic ion jet are observed at X3. This category has U_ψ reversals, but no plasma outflow jet reversal. Electron-only reconnection with only one jet is also reported in simulations of shock-driven turbulence (Bessho et al. 2020).

7. Application to Heliospheric Plasmas

Application of the MFT method to heliospheric plasmas requires the following conditions: (i) $k_\parallel \ll k_\perp$, where "$\parallel$" is along the background magnetic field (guide field), and (ii) the reconnection magnetic fields primarily reside on a local reconnection plane. $k_\parallel \ll k_\perp$ is based on $k_\parallel/k_\perp \ll \delta E_\parallel/\delta E_\perp$ for deriving $\partial_t \psi$ (Section 2), a condition well satisfied in the simulation. Equation (1) is then a good approximation of U_ψ, even in 3D systems. Physically, this represents quasi-planar reconnection with parallel length scales much longer than perpendicular. $k_\parallel \ll k_\perp$ is well satisfied in the cascade of kinetic Alfvén wave turbulence (Cho & Lazarian 2004; Schekochihin et al. 2009), which is consistent with solar wind and magnetosheath observations (Alexandrova et al. 2008, 2009; Sahraoui et al. 2013; Chen 2016; Chen & Boldyrev 2017). The model of planar reconnection is adopted by the local current sheet (LMN) coordinate (Sonnerup & Cahill 1967), commonly used in space reconnection observations. Observations of reconnection in small-scale current sheets in the turbulent magnetosheath are consistent with this model (e.g., Phan et al. 2018; Wilder et al. 2018). Thus, the conditions for applying MFT is expected to be realistic for reconnection in heliospheric turbulence. Recent 3D PIC simulations further show that a long extended X-line, satisfying $k_\parallel \ll k_\perp$, easily arising in sub-ion-scale current sheets in 3D (Li et al. 2020), also favors reconnection activity (Liu et al. 2019; Huang et al. 2020).

8. Conclusion

The MFT method is a new way of identifying reconnection X-points in turbulent plasmas. It captures bidirectional inflows and outflows of magnetic flux at the X-points to signify reconnection, even without bidirectional plasma outflow jets. $\nabla \cdot U_\psi$ is suitable for use in multispacecraft missions such as MMS. The first application to a 2D gyrokinetic turbulence simulation demonstrates the capability of this method in clearly capturing active reconnection signatures, as an inflow-outflow pattern or a quadrupolar structure in $\nabla \cdot U_\psi$. It also reveals a new category of reconnection in turbulence beyond electron-only reconnection. This method has the potential to replace the plasma outflow jet reversal signature for reconnection. Applications to 3D simulations and helisopheric observations from spacecraft missions will present new opportunities to study the role of reconnection and identify new types of reconnection in turbulence.

Appendix

Two supplementary figures are available. Figure A1 shows the turbulent cascade in the dissipation range in the magnetic energy spectrum. Figure A2 shows the fluctuating in-plane ion flow velocity δu_i for X3.
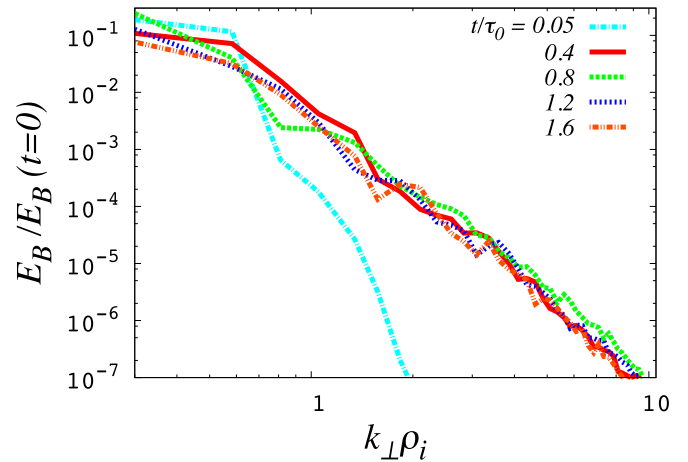

Figure A1. Evolution of the magnetic energy spectrum as a function of scale, showing a developed turbulent cascade in the dissipation range.
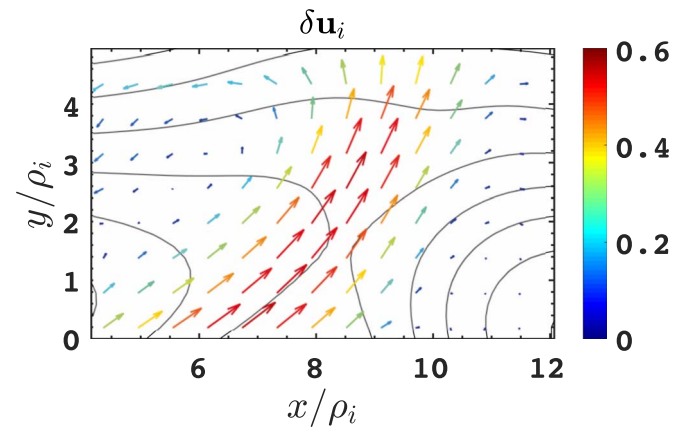

Figure A2. Ion flow velocity δu_i for X3, showing one outflow jet in ions. Compare with the electron flow velocity in Figure 4(c). δu_i is normalized to the ion thermal speed v_{ti}.

ORCID iDs

Tak Chu Li ⓘ https://orcid.org/0000-0002-6367-1886
Yi-Hsin Liu ⓘ https://orcid.org/0000-0001-5880-2645
Yi Qi ⓘ https://orcid.org/0000-0002-0959-3450

References

Abel, I. G., Barnes, M., Cowley, S. C., Dorland, W., & Schekochihin, A. A. 2008, PhPl, 15, 122509
Alexandrova, O., Lacombe, C., & Mangeney, A. 2008, AnGeo, 26, 3585
Alexandrova, O., Saur, J., Lacombe, C., et al. 2009, PhRvL, 103, 165003
Barnes, M., Abel, I. G., Dorland, W., et al. 2009, PhPl, 16, 072107
Bessho, N., Chen, L. J., Wang, S., et al. 2020, PhPl, 27, 092901
Boldyrev, S., & Loureiro, N. F. 2017, ApJ, 844, 125
Burch, J. L., Tobert, R. B., Phan, T., et al. 2016, Sci, 352, aaf2939
Cassak, P. A., & Shay, M. A. 2007, PhPl, 14, 102114
Chen, C. H. K. 2016, JPlPh, 82, 535820602
Chen, C. H. K., & Boldyrev, S. 2017, ApJ, 842, 122
Cho, J., & Lazarian, A. 2004, ApJL, 615, L41
Dahlburg, R. B., & Picone, J. M. 1989, PhFlB, 1, 2153
Dmitruk, P., Matthaeus, W. H., & Seenu, N. 2004, ApJ, 617, 667
Franci, L., Cerri, S. S., Califano, F., et al. 2017, ApJL, 850, L16
Frieman, E. A., & Chen, L. 1982, PhFl, 25, 502
Grauer, R., & Marliani, C. 2000, PhRvL, 84, 4850
Haggerty, C. C., Parashar, T. N., Matthaeus, W. H., et al. 2017, PhPl, 24, 102308
Hasegawa, H., Denton, R. E., Genestreti, K. J., et al. 2020, Natur, submitted

Howes, G. G. 2016, ApJL, 82, L28
Howes, G. G., Cowley, S. C., Dorland, W., et al. 2006, ApJ, 651, 590
Howes, G. G., Dorland, W., Cowley, S. C., et al. 2008, PhRvL, 100, 065004
Howes, G. G., McCubbin, A. J., & Klein, K. G. 2018, JPlPh, 84, 905840105
Howes, G. G., TenBarge, J. M., Dorland, W., et al. 2011, PhRvL, 107, 035004
Huang, K., Liu, Y.-H., Lu, Q., & Hesse, M. 2020, GeoRL, 47, e88147
Karimabadi, H., Roytershteyn, V., Wan, M., et al. 2013, PhPl, 20, 012303
Kobayashi, S., Rogers, B. N., & Numata, R. 2014, PhPl, 21, 040704
Li, T. C., Howes, G. G., Klein, K. G., Liu, Y.-H., & TenBarge, J. M. 2019, JPlPh, 85, 905850406
Li, T. C., Howes, G. G., Klein, K. G., & TenBarge, J. M. 2016, ApJL, 832, L24
Li, T. C., Liu, Y.-H., Hesse, M., & Zou, Y. 2020, JGRA, 125, e27094
Liu, Y.-H., & Hesse, M. 2016, PhPl, 23, 060704
Liu, Y.-H., Hesse, M., Guo, F., Li, H., & Nakamura, T. K. M. 2018, PhPl, 25, 080701
Liu, Y.-H., Li, T. C., Hesse, M., et al. 2019, JGRA, 124, 2819
Loureiro, N. F., & Boldyrev, S. 2017a, PhRvL, 118, 245101
Loureiro, N. F., & Boldyrev, S. 2017b, ApJ, 850, 182
Mallet, A., Schekochihin, A. A., & Chandran, B. D. G. 2017a, MNRAS, 468, 4862
Mallet, A., Schekochihin, A. A., & Chandran, B. D. G. 2017b, JPlPh, 83, 905830609
Markovskii, S. A., & Vasquez, B. J. 2011, ApJ, 739, 22
Mininni, P. D., Pouquet, A. G., & Montgomery, D. C. 2006, PhRvL, 97, 244503
Nielson, K. D., Howes, G. G., & Dorland, W. 2013, PhPl, 20, 072303
Numata, R., Dorland, W., Howes, G. G., et al. 2011, PhPl, 18, 112106
Numata, R., Howes, G. G., Tatsuno, T., Barnes, M., & Dorland, W. 2010, JCoPh, 229, 9347
Numata, R., & Loureiro, N. F. 2015, JPlPh, 81, 305810201
Osman, K. T., Matthaeus, W. H., Greco, A., & Servidio, S. 2011, ApJL, 727, L11
Osman, K. T., Matthaeus, W. H., Wan, M., & Rappazzo, A. F. 2012, PhRvL, 108, 261102
Parashar, T. N., Shay, M. A., Cassak, P. A., & Matthaeus, W. H. 2009, PhPl, 16, 032310
Parashar, T. N., Vasquez, B. J., & Markovskii, S. A. 2014, PhPl, 21, 022301

Perri, S., Goldstein, M. L., Dorelli, J. C., & Sahraoui, F. 2012, PhRvL, 109, 191101
Phan, T. D., Eastwood, J. P., Shay, M. A., et al. 2018, Natur, 557, 202
Picone, J. M., & Dahlburg, R. B. 1991, PhFlB, 3, 29
Politano, H., Pouquet, A., & Sulem, P. L. 1989, PhFlB, 1, 2330
Politano, H., Pouquet, A., & Sulem, P. L. 1995, PhPl, 2, 2931
Retinò, A., Sundkvist, D., Vaivads, A., et al. 2007, NatPh, 3, 236
Sahraoui, F., Huang, S. Y., Belmont, G., et al. 2013, ApJ, 777, 15
Schekochihin, A. A., Cowley, S. C., Dorland, W., et al. 2009, ApJS, 182, 310
Servidio, S., Matthaeus, W. H., Shay, M. A., et al. 2010, PhPl, 17, 032315
Servidio, S., Matthaeus, W. H., Shay, M. A., Cassak, P. A., & Dmitruk, P. 2009, PhRvL, 102, 115003
Shay, M. A., Haggerty, C. C., Matthaeus, W. H., et al. 2018, PhPl, 25, 012304
Sonnerup, B. U. Ö., & Cahill, L. J., Jr. 1967, JGR, 72, 171
Stawarz, J. E., Eastwood, J. P., Phan, T. D., et al. 2019, ApJL, 877, L37
Sundkvist, D., Retinò, A., Vaivads, A., & Bale, S. D. 2007, PhRvL, 99, 025004
Tatsuno, T., Dorland, W., Schekochihin, A. A., et al. 2009, PhRvL, 103, 015003
TenBarge, J. M., Daughton, W., Karimabadi, H., Howes, G. G., & Dorland, W. 2014, PhPl, 21, 020708
TenBarge, J. M., & Howes, G. G. 2012, PhPl, 19, 055901
TenBarge, J. M., & Howes, G. G. 2013, ApJL, 771, L27
TenBarge, J. M., Howes, G. G., & Dorland, W. 2013, ApJ, 774, 139
Vasyliunas, V. M. 1975, RvGSP, 13, 303
Vech, D., Mallet, A., Klein, K. G., & Kasper, J. C. 2018, ApJL, 855, L27
Vörös, Z., Yordanova, E., Varsani, A., et al. 2017, JGRA, 122, 442
Wan, M., Matthaeus, W. H., Karimabadi, H., et al. 2012, PhRvL, 109, 195001
Wan, M., Matthaeus, W. H., Servidio, S., & Oughton, S. 2013, PhPl, 20, 042307
Wilder, F. D., Ergun, R. E., Burch, J. L., et al. 2018, JGRA, 123, 6533
Wu, P., Perri, S., Osman, K., et al. 2013, ApJL, 763, L30
Yordanova, E., Vörös, Z., Varsani, A., et al. 2016, GeoRL, 43, 5969
Zenitani, S., Hesse, M., Kimas, A., & Kuznetsova, M. 2011, PhRvL, 106, 195003
Zhdankin, V., Uzdensky, D. A., Perez, J. C., & Boldyrev, S. 2013, ApJ, 771, 124